nature nanotechnology

ARTICLES

PUBLISHED ONLINE: 30 MARCH 2014 | DOI: 10.1038/NNANO.2014.38

Multifunctional wearable devices for diagnosis and therapy of movement disorders

Donghee Son[1,2†], Jongha Lee[1,2†], Shutao Qiao[3], Roozbeh Ghaffari[4], Jaemin Kim[1,2], Ji Eun Lee[1,2], Changyeong Song[1,2], Seok Joo Kim[1,2], Dong Jun Lee[1,2], Samuel Woojoo Jun[1,2], Shixuan Yang[3], Minjoon Park[1,2], Jiho Shin[1,2], Kyungsik Do[1,2], Mincheol Lee[1,2], Kwanghun Kang[1,2], Cheol Seong Hwang[5], Nanshu Lu[3], Taeghwan Hyeon[1,2] and Dae-Hyeong Kim[1,2*]

Wearable systems that monitor muscle activity, store data and deliver feedback therapy are the next frontier in personalized medicine and healthcare. However, technical challenges, such as the fabrication of high-performance, energy-efficient sensors and memory modules that are in intimate mechanical contact with soft tissues, in conjunction with controlled delivery of therapeutic agents, limit the wide-scale adoption of such systems. Here, we describe materials, mechanics and designs for multifunctional, wearable-on-the-skin systems that address these challenges via monolithic integration of nanomembranes fabricated with a top-down approach, nanoparticles assembled by bottom-up methods, and stretchable electronics on a tissue-like polymeric substrate. Representative examples of such systems include physiological sensors, non-volatile memory and drug-release actuators. Quantitative analyses of the electronics, mechanics, heat-transfer and drug-diffusion characteristics validate the operation of individual components, thereby enabling system-level multifunctionalities.

Wearable sensor-laden devices that provide continuous measurement of key physiological parameters, coupled with data storage and drug delivery, constitute a radical advance in personal healthcare. Health-monitoring devices in the form of wearable pads, wrist-bands and straps that provide long-term continuous recordings of electrophysiological activity and acute physiological responses have significantly improved our understanding of diseases, including heart failure[1], epilepsy[2] and Parkinson's disease[3,4]. Although conventional monitoring devices capture compelling physiological data, the form factors of existing devices restrict seamless integration with the skin[1], giving rise to wearability challenges and signal-to-noise limitations[2,4].

Electronic systems that incorporate inorganic and organic nanomaterials in flexible and stretchable configurations[5–9] are particularly powerful alternatives to bulky health-monitoring devices, providing improvements in comfort and reduced social stigma, which together drive compliance. This emerging class of electronics includes sensors, light-emitting diodes and associated circuit components that interface with internal organs (such as the heart[10,11] and brain[12,13]) and skin[14] (or artificial skin scaffolds[15–17]). However, a key constraint of these flexible and stretchable electronics for wearable biomedical devices lies in their inability to store recorded data in memory modules during continuous, long-term monitoring. Another desirable feature missing in emerging wearable devices is the ability to deliver advanced therapy in response to diagnostic patterns present in the collected data[18].

Resistive random access memory (RRAM), constructed from oxide nanomembranes, is an emerging class of high-performance non-volatile memory[19–21]. RRAM devices are composed of stiff and brittle electronic materials, which tend to be mechanically incompatible with curvilinear, dynamically deforming, soft tissues. Although organic non-volatile memory has enabled the development of flexible data-storage devices[22,23], there remain restrictions, such as high power consumption, insufficient reliability and lack of stretchability.

Here, we demonstrate wearable bio-integrated systems with optimized performance of data storage, diagnostics and drug delivery functionality in stretchable formats, enabled by the integration of bottom-up nanoparticles and top-down nanomembranes. This novel nanoparticle-integrated system includes low-power-consumption, non-volatile resistance memory devices, together with programmable thermal actuators for controlled transdermal nanoparticle-assisted drug delivery, and well-known stretchable sensors (e.g. temperature and strain sensors). We establish new engineering design rules and guides for multifunctional healthcare systems. Potential applications of these wearable patches range from monitoring physiological cues of motion-related neurological disorders (movement disorders) to controlled drug delivery in response to diagnostic feedback (Supplementary Fig. 1). For example, let us suppose that a Parkinson's disease patient wears the current multifunctional device. Movement disorders such as tremors can be measured (using silicon nanomembrane (Si NM) strain sensors), and the monitored data stored in integrated memory devices (gold nanoparticle (Au NP) RRAMs). The pattern of stored data will be analysed and categorized into specific disease modes, and the corresponding feedback therapy (drug delivery from mesoporous-silica (m-silica) nanoparticles) will proceed transdermally at optimized rates through thermal stimuli (heater). The skin temperature

[1]Center for Nanoparticle Research, Institute for Basic Science (IBS), Seoul 151-742, Republic of Korea, [2]School of Chemical and Biological Engineering and Institute of Chemical Processes, Seoul National University, Seoul 151-742, Republic of Korea, [3]Center for Mechanics of Solids, Structures and Materials, Department of Aerospace Engineering and Engineering Mechanics, Texas Materials Institute, University of Texas at Austin, 210 E 24th Street, Austin, Texas 78712, USA, [4]MC10 Inc., 9 Camp Street, Cambridge, Massachusetts 02140, USA, [5]WCU Hybrid Materials Program, Department of Materials Science and Engineering and Inter-university Semiconductor Research Center, Seoul National University, Seoul 151-744, Republic of Korea. †These authors contributed equally to this work. *e-mail: dkim98@snu.ac.kr

© 2014 Macmillan Publishers Limited. All rights reserved.

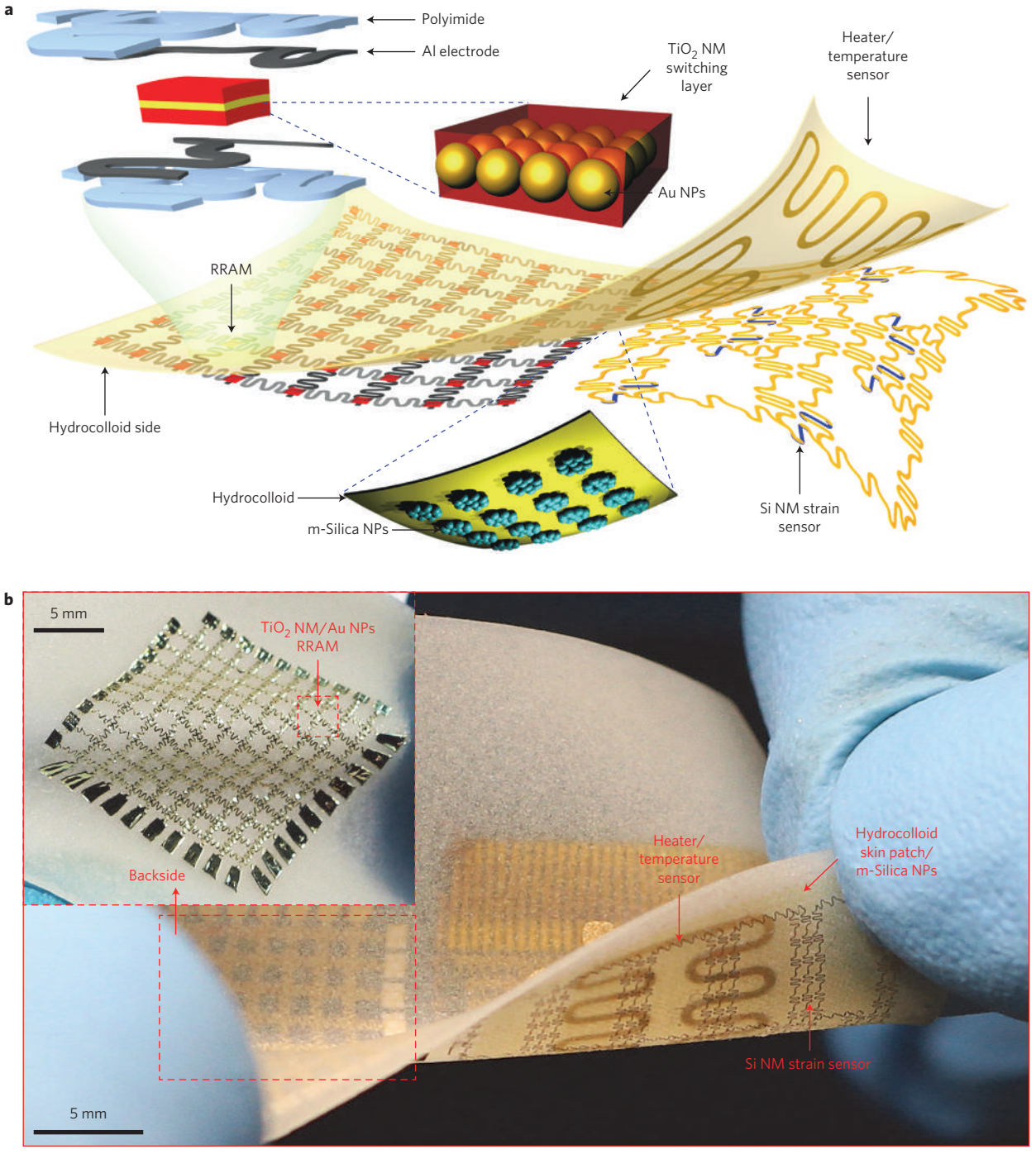

Figure 1 | Wearable electronic patch composed of data storage modules, diagnostic tools and therapeutic actuating elements. a, Wearable memory array consisting of a TiO_2 NM–Au NPs–TiO_2 NM switching layer and Al electrodes (top left inset: layer information). The memory array was transfer-printed on the bottom side of an elastomeric hydrocolloid skin patch. The electroresistive heater/temperature sensor was fabricated on the top-side of the patch, with the Si strain sensor on the opposite side. The m-silica NP array was transfer-printed on the hydrocolloid side of the patch. **b**, Corresponding image of **a**, showing the wearable bio-integrated system. Inset: Wearable 10 × 10 RRAM array on the hydrocolloid side of the patch.

will be simultaneously monitored (temperature sensor) to prevent skin burns during thermal control of the drug delivery rate.

System description

Figure 1 presents a schematic illustration and image of a representative wearable bio-integrated system containing single-crystal Si NM (~80 nm) strain sensors, a temperature sensor, a TiO_2 NM (~66 nm) RRAM array, and electroresistive heaters. These multifunctional arrays of sensors and memory are heterogeneously fabricated and transfer-printed onto an elastomeric hydrocolloid patch (Derma-Touch, Kwang-Dong Pharmaceutical, Supplementary Fig. 2). To minimize bending-induced strains, the switching TiO_2 NM layer containing Au NPs is sandwiched by identical polyimide layers (~1.2 μm) to be located on the neutral mechanical plane (top left, Fig. 1a)[6]. Thickness control of the inorganic active layers on a scale within tens of nanometres further decreases flexural rigidity and induced strain[24]. m-Silica nanoparticles loaded with therapeutic drugs are transferred onto the hydrocolloid side of the

© 2014 Macmillan Publishers Limited. All rights reserved.

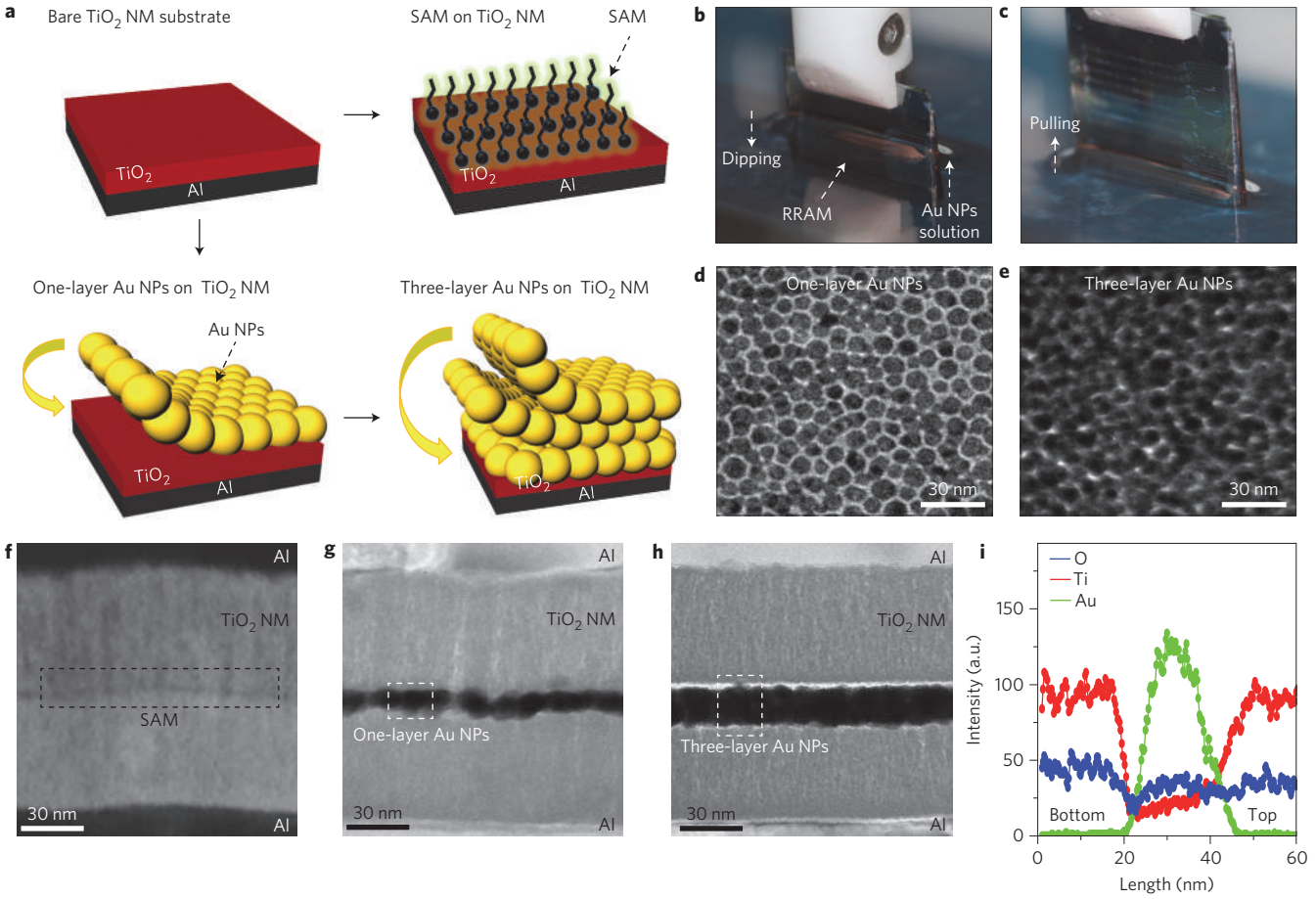

Figure 2 | Langmuir–Blodgett assembly and SAM functionalization process. a, Schematic diagram for Langmuir–Blodgett assembly and SAM functionalization. Au NPs were coated onto the switching TiO_2 NM using the Langmuir–Blodgett assembly process. The number of Au NP layers ranges from one to three. **b**,**c**, Images of Langmuir–Blodgett assembly process during dipping (**b**) and pulling (**c**). **d**,**e**, Top-view TEM images of one-layer Au NPs (**d**) and three-layer Au NPs (**e**). **f**, Cross-sectional STEM image of MISIM structure. **g**,**h**, Cross-sectional TEM images of MINIM of one-layer Au NPs (**g**) and MINIM of three-layer Au NPs (**h**). **i**, Energy-dispersive X-ray spectroscopy profile showing the thickness of three-layer Au NPs in MINIM.

skin patch (bottom middle, Fig. 1a). Ultrathin serpentines and low-modulus hydrocolloids together enable intimate mechanical contact with the skin[14]. The inset of Fig. 1b highlights a 10×10 RRAM array in a serpentine network, which is integrated with sensors that transmit analogue outputs. Therapeutic drugs loaded on m-silica nanoparticles are diffused into the dermis[25], where the diffusion rate is controlled by the temperature of the hydrocolloid elastomer, which is modulated by the heater. Temperature sensors offer *in situ* temperature feedback to warn of skin burns.

Integration of nanoparticles

The fabrication process (Supplementary Fig. 2) began with the formation of a TiO_2 NM on Al electrodes[26]. The Langmuir–Blodgett assembly process provided uniform-sized Au NPs (diameter of ~12 nm)[27–29] on the TiO_2 NM (Fig. 2a). Figure 2b,c presents images of the Langmuir–Blodgett process (Fig. 2b, dipping; Fig. 2c, pulling) and transmission electron microscopy (TEM) images of assembled one-layer (Fig. 2d) and three-layer (Fig. 2e) Au NPs. The number of assembly layers could be controlled by the number of dipping/pulling cycles[30]. Instead of Au NP layers, a self-assembled monolayer (SAM; stearic acid) could be coated to check the ligand effect on memory performance (Fig. 2a and Supplementary Fig. 3). Cross-sectional scanning TEM (STEM) and TEM images of fabricated devices are shown in Fig. 2f–h. Metal–insulator–SAM–insulator–metal (MISIM, Fig. 2f), metal–insulator–NP–insulator–metal (MINIM, Fig. 2g) with one-layer-Au NPs (~12 nm) and MINIM with closely packed three-layer-Au NPs (~26 nm, Fig. 2h) are represented, respectively. An energy-dispersive X-ray spectroscopy profile of the cross-section also confirms the thickness of three-layer Au NPs (Fig. 2i). The closely packed monolayer assembly during the Langmuir–Blodgett process plays an important role in achieving device-to-device uniformity in a matrix configuration, as well as precise thickness control of multiple monolayers[27].

Characterization of RRAM

To characterize electrical performance, we collected bipolar current/voltage (I–V) curves for the metal-insulator-metal (MIM), MISIM and MINIM structures (Fig. 3a). The inset in Fig. 3a illustrates the biasing sequences. The initial states are in the high-resistance state, and application of a negative voltage ('set') causes a shift to the low-resistance state. Positive voltage ('reset') then switches the structures back to the high-resistance state. The I–V characteristics of MIM and MISIM are almost identical, while the incorporation of one-layer Au NPs into the TiO_2 NM layer decreases the set and reset currents by nearly one order of magnitude relative to those of MIM. The current levels are further reduced (by three orders of magnitude) in three-layer Au NP MINIM. These results imply that the uniform assembly of Au NPs in the active layer plays a critical role in reducing power consumption, and stearic acid ligands have little effect on current reduction. This low power consumption property is important for the long-term operation of wearable devices.

© 2014 Macmillan Publishers Limited. All rights reserved.

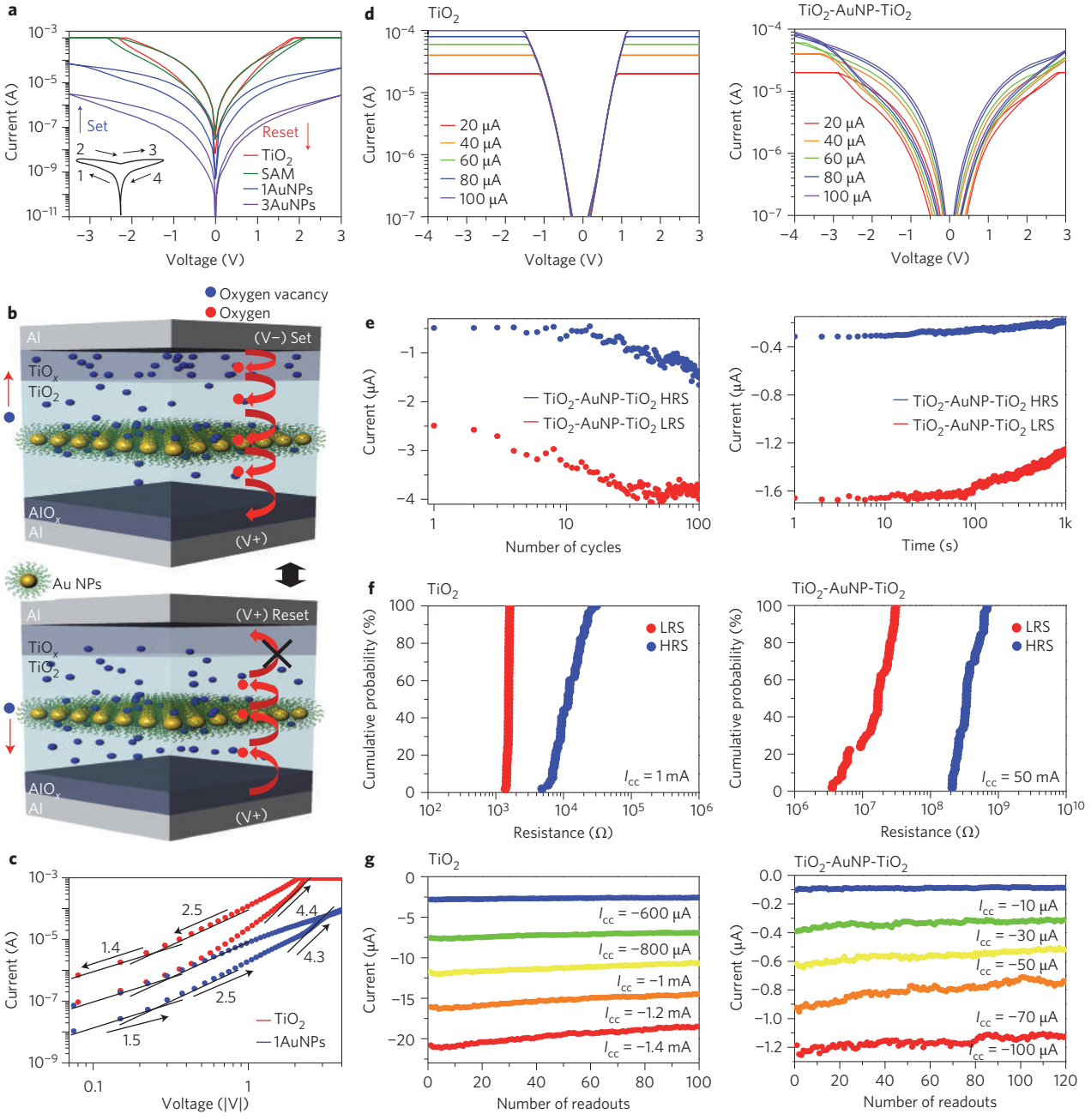

Figure 3 | Electrical characteristics of RRAMs in MIM, MISIM and MINIM structures. a, *I*–*V* characteristics of the bipolar resistive switching of MIM, MISIM and MINIM structures. Inset: Switching sequence. **b**, Schematic of low-current resistive switching due to Au NP-induced traps. Red curved arrows indicate electron flow in MINIM and red flat arrows indicate oxygen vacancy flow. **c**, Double-logarithmic plots of *I*–*V* curves in MIM and MINIM. Numbers indicate the slope, with slope increasing for larger voltages. **d**, *I*–*V* characteristics with compliance currents below ~100 μA in MIM (left) and MINIM (right). **e**, Reliability test (endurance and retention: left and right, respectively) of MINIM. Resistance values are measured at −0.5 V. **f**, Cumulative probability plot in MIM and MINIM, showing the uniformity within the array. **g**, Multilevel-cell operation in MIM (left) and MINIM (right) with discrete compliance currents (I_{cc}).

Figure 3b presents a schematic diagram of the low current switching due to Au NP-induced traps (for details see Supplementary Section 1.1). Figure 3c shows log *I*–log *V* curves, highlighting the negative voltage regions. The conduction mechanism in MINIM is similar to that of MIM (the slopes of both MIM and MINIM vary from ~1 to ~2, and >2 with increasing voltages), which follows the trap-controlled space-charge-limited-current (SCLC) theory[31,32]. Figure 3d shows *I*–*V* curves with different compliance currents (I_{cc}) for MIM (left) and MINIM (right). MINIM exhibits better on/off ratios than MIM and MISIM (Supplementary Fig. 4a), with compliance currents of <100 μA. The reliability (endurance and retention) of MINIM, MIM and MISIM is shown in Fig. 3e and Supplementary Fig. 3b,c, respectively (Supplementary Section 1.2). The endurance is reliable, with little degradation in consecutive sweeping over 100 cycles (Fig 3e, left) and the good retention up to 1,000 s is confirmed at room temperature (Fig 3e, right). Figure 3f presents the cumulative probability plot of MIM and MINIM, which shows uniform switching of the array (Supplementary Section 1.3). Although the on/off ratio in the current RRAM demonstrations can be further improved, data storage in a 10 × 10 matrix configuration was effective. Further improvements can be achieved by incorporating high-quality

© 2014 Macmillan Publishers Limited. All rights reserved.

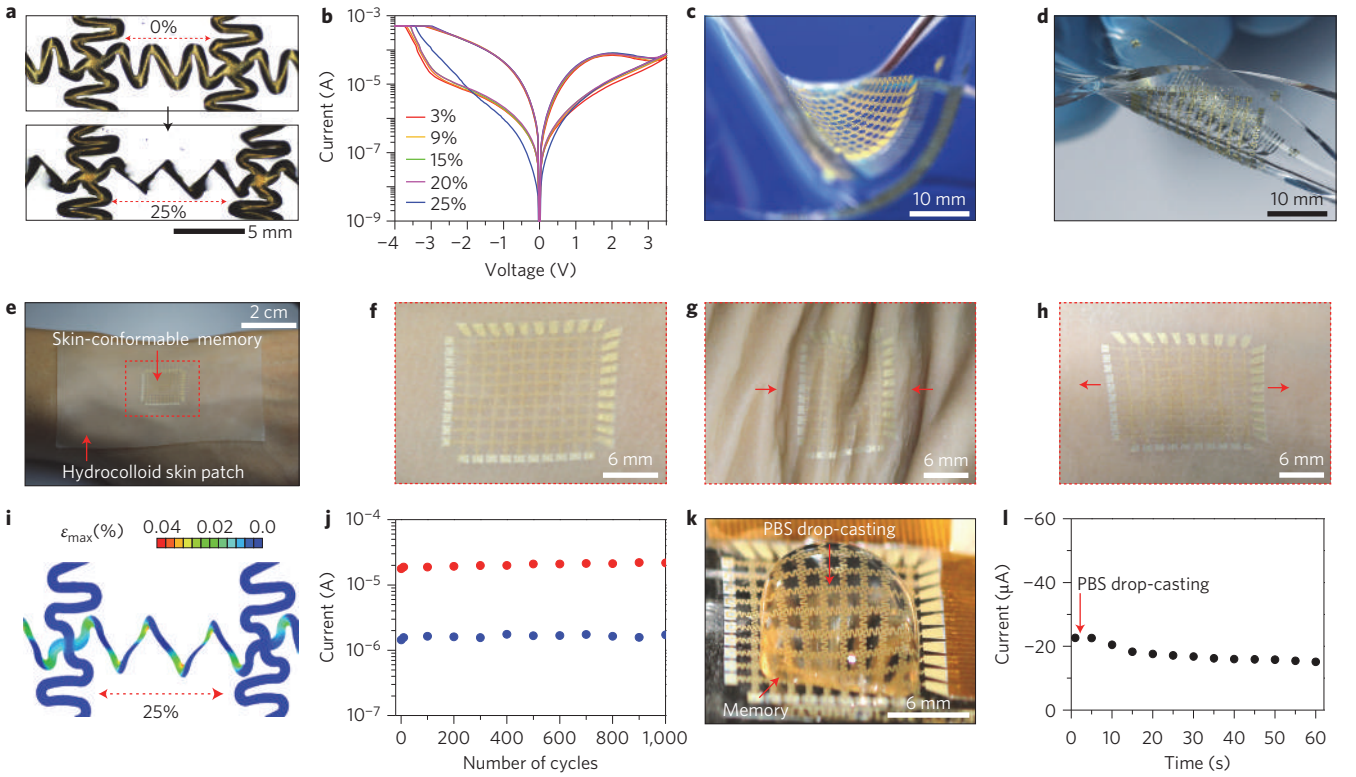

Figure 4 | Skin-conformable RRAM array with mechanical stretchability and chemical stability. a, Microscope images of stretched memory (~25%) on PDMS. **b**, *I–V* characteristics of the stretched memory at different strains (~3–25%). **c**,**d**, Stretchable RRAM array in bent state (**c**) and twisted state (**d**). **e**, Skin-conformable memory devices on a wrist. **f**–**h**, Magnified views under no strain (**f**), compression (**g**) and tension (**h**). Red arrows indicate direction of strain. **i**, FEM of strain distribution in stretched RRAM. **j**, Resistance change between low-resistance state (LRS, red dots) and high-resistance state (HRS, blue dots) at a read voltage of −0.5 V during 1,000 stretching cycles (~30%). **k**,**l**, Waterproof test in phosphate buffered solution (PBS) (**k**) and read current (**l**).

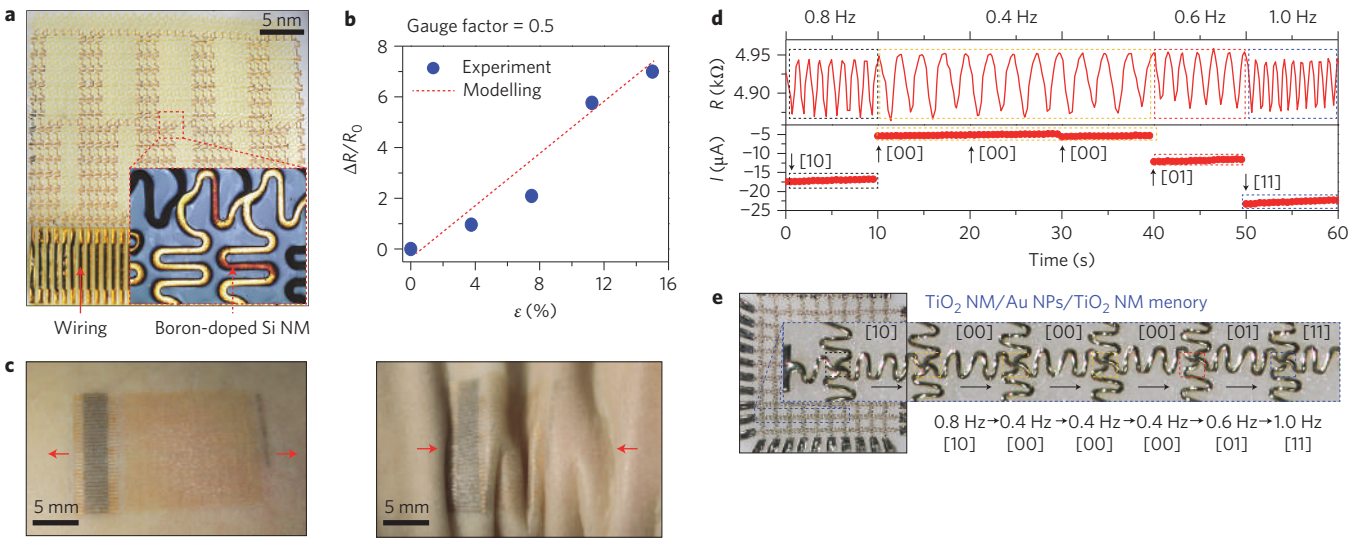

Figure 5 | *In vivo* motion detection and data storage test. a, Images of a Si NM strain sensor. Boron-doped Si NM is positioned along *x*- and *y*-axes (inset). **b**, Plot of percentage change in resistance versus strain for calculation of the gauge factor. **c**, Images of strain measurement on the wrist under tension (left) and compression (right). Red arrows indicate direction of strain. **d**, Top: Plot of time-dependent change in resistance in the Si strain gauge caused by simulated hand tremors at frequencies of 0.8, 0.4, 0.6 and 1 Hz. Bottom: Plot illustrating the multilevel-cell operation of memory cells. **e**, The frequency of strain data is monitored and classified into four levels: [00], [01], [10] and [11]. The dotted rectangles in black, orange, red and blue correspond to levels [00], [01], [10] and [11], respectively. Data are written on a MINIM memory cell and read repeatedly for 10 s.

Al_2O_3 instead of a native alumina layer, or by depositing additional metal (tungsten or nickel) layers between the Al (top electrode) and TiO_2 NM[33]. Multilevel-cell operations indicate multidata storage in a single cell with discrete compliance currents that result in discrete resistance levels (Fig. 3d). Different resistances enable multiple information to be stored in a single cell (Fig. 3g). Multilevel-cell operation with current levels below −100 μA is performed in MINIM and data are conserved over 100 read operations.

© 2014 Macmillan Publishers Limited. All rights reserved.

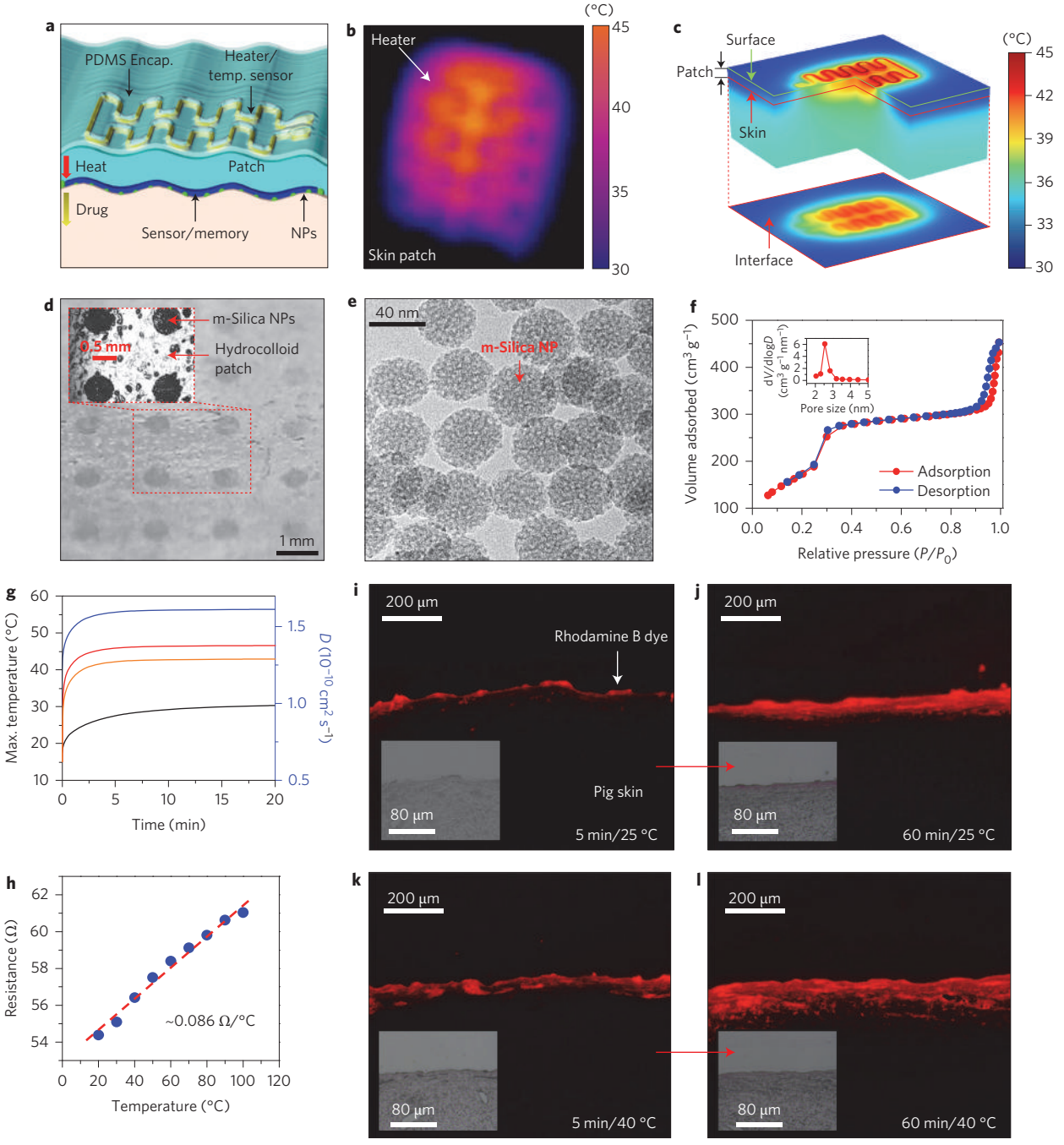

Figure 6 | Controlled transdermal drug delivery using the electroresistive heater and drug-loaded m-silica NPs. a, Schematic illustration of controlled transdermal drug delivery from hydrocolloid and m-silica NPs by thermal actuation. **b**, Temperature distribution measurement of the heater on the skin patch using an infrared camera. **c**, FEM of the three-dimensional thermal profile of a heater on the patch and at the interface between the patch and the human skin. **d**, High-resolution camera image showing an array of m-silica NPs. Inset: Microscope image. **e**, TEM image of m-silica NPs. **f**, Surface area calculation through the measurement of N_2 adsorption and desorption isotherms at 77 K. Inset: Pore volume of the m-silica NPs using the Barrett–Joyner–Halenda method. **g**, Plots of maximum temperature as a function of time on the heater surface (red), on the interface between the skin and patch (orange), and on the interface without heating (black). The right *y*-axis shows the diffusion coefficient exponentially increasing with temperature (blue). **h**, Characterization plot of the temperature sensor. The dashed red line implies a linear approximation of the blue data points. **i**,**j**, Cross-sectional fluorescence images of the pig skin before the diffusion of Rhodamine B dyes at 25 °C (**i**) and after diffusion (**j**). **k**,**l**, Cross-sectional fluorescence images of the pig skin before the diffusion of Rhodamine B dyes at 40 °C (**k**) and after diffusion (**l**). The insets in **i**–**l** are optical microscope images of the same pig skin samples shown in the main panels before they were dyed with Rhodamine B.

Reliability of wearable electronic system

The mechanical and chemical stability of wearable memory is demonstrated in Fig. 4. Optical microscope images of the stretchable memory and corresponding characterization data during stretching are shown in Fig. 4a,b, respectively. When stretched to ~25% (the strain limitation of human epidermis is ~20%)[14], the memory device shows stable electrical operation. The stretchable memory array can survive both bending (Fig. 4c) and twisting (Fig. 4d) and can conform to and deform with human skin (Fig. 4e–h). Figure 4i and Supplementary Fig. 5 show finite element modelling

© 2014 Macmillan Publishers Limited. All rights reserved.

(FEM, Supplementary Section 1.4) results of the strain distribution of the active layer (TiO_2 NM). By positioning the nanometre-thick membrane and nanoparticles on the neutral mechanical plane and by using serpentine designs, the induced strain is kept below 0.1% in the switching layers and below 0.05% in the serpentine interconnects. The skin-conformable memory performs well with minimal signal degradation, even after 1,000 stretching cycles (~30% strain, Fig. 4j). Figure 4k shows an image of the memory device immersed in PBS without significant current variation (Fig. 4l), indicating that the encapsulation layer is capable of blocking perspiration uptake.

Recording muscle activity

Figure 5a presents an array of stretchable strain sensors based on a Si NM (inset and Supplementary Fig. 6), as a representative example of wearable sensors in conjunction with collocated memory. The strain gauges have an effective gauge factor of ~0.5 (Fig. 5b), consistent with gauge factor estimates derived analytically (Supplementary Section 1.5). Because of the ultrathin serpentine interconnects, the sensors conform well to the skin during repeated exposure to tension and compression on a human wrist (Fig. 5c). This particular demonstration emulates tremor modes that manifest in epilepsy[2] and Parkinson's disease[3] (Fig. 5d). Detection of different tremor frequencies serves as a powerful way to monitor and diagnose these movement disorders. A data registering scheme is described in Supplementary Fig. 7, where the data captured from the movements is stored in separate memory cells every 10 s, using a custom-made software program (see Methods). Representative frequencies corresponding to different frequency bands (0–0.5, 0.5–0.7, 0.7–0.9 and >0.9 Hz) are stored as four different levels (Fig. 5e) on the basis of multilevel-cell operation (Fig. 3g) of MINIM wearable memory. The written data are then read every 0.5 s, allowing physicians to monitor patient health conditions, analyse patterns, and diagnose (Supplementary Fig. 1).

Controlled delivery of therapeutic agents

A compelling application for sensing and data storage is to use the stored information to trigger the onset of therapy. One possible mode of use is to feed recorded data through a control circuit that recognizes the characteristic patterns of disease; this, in turn, triggers/controls drug release (Fig. 6a, Supplementary Fig. 1). We used m-silica nanoparticles as a drug-containing and drug-delivery vehicle[34,35] (Fig. 6d–f) and an electroresistive heater/temperature sensor as a diffusion-accelerating/temperature-monitoring element (Fig. 6b,c,g,h) for controlled transdermal drug delivery (Fig. 6i)[25]. The m-silica nanoparticles loaded with drugs were transfer-printed onto the sticky side of the patch (Fig. 6d, Supplementary Fig. 8a) using a structured polydimethylsiloxane (PDMS) stamp (Supplementary Fig. 8b). These nanoparticles, which have nanopores (Fig. 6e), have a large surface area for drug adsorption (Fig. 6f). Figure 6b shows the thermal gradient image (infrared camera measurements) of an electroresistive heater on the patch surface. Figure 6c shows the corresponding FEM analysis, emphasizing the three-dimensional thermal profile of the device on multilayered human skin, and demonstrating the delivery of sufficient heat to the skin and nanoparticles (Supplementary Fig. 9). The heat generated by the heater degrades the physical bonding between the nanoparticles and the drugs, and pharmacological agents loaded in the nanoparticles are thus diffused transdermally. FEM simulation confirmed the increase of diffusion rates by heating (Fig. 6g, Supplementary Section 1.6). The sensitivity of the temperature sensor (Fig. 6h) was ~0.086 Ω/°C, which is similar to that in previous reports of thermal monitoring[36]. Further improvements in sensitivity could be achieved by optimizing the materials and the design of the thermistor. Also, high uniformity of the temperature sensor can be obtained by precise control of the metal evaporation process. The temperature sensor was able to monitor the maximum temperature on the epidermis, and the skin could be protected from getting burnt (<43 °C) by using a control unit programmed by the Labview software. Transdermal drug delivery could be indirectly visualized by fluorescence microscope imaging of a dye (Rhodamine B) diffusing into the pig skin at room temperature (25 °C, Fig. 6i,j) and at elevated temperatures (40 °C, Fig. 6k,l) (Supplementary Section 1.7). The penetration depth of the dye into the pig skin at room temperature is shallower than that at elevated temperature, implying accelerated diffusion by thermal actuation.

Conclusions

The materials, mechanics and electronics strategies for wearable biomedical systems using stretchable designs and heterogeneous integration of nanomembranes and nanoparticles provide opportunities for advanced diagnostics and drug delivery. This platform overcomes the limitations of conventional wearable devices and has the potential to improve compliance, data quality and the efficacy of current clinical procedures. Analytical modelling and FEM analysis validate the mechanical, thermal and kinetic functionalities of the individual components and lay the foundation for rationalized designs and analysis. Together with the sensing, memory and therapeutic modules presented here, future developments towards achieving completely wire-free devices might include energy storage units (for example, battery or wireless power transmission), central control units (for example, a microprocessor) and additional wireless communication units in a stretchable format[18,36,37], thereby realizing interactive and remote healthcare.

Methods

Fabrication and electrical measurement of MINIM (Al–TiO_2 NM–Au NPs–TiO_2 NM–Al) memory on a wearable skin patch. A schematic description of the fabrication processes is provided in Supplementary Fig. 2. Thin layers of poly(methyl methacrylate) (PMMA) (A11, Microchem; ~1 μm, spin-coated at 3,000 r.p.m. for 30 s) and a precursor solution of polyimide (PI) (polyamic acid, Sigma Aldrich; ~1.2 μm, spin-coated at 4,000 r.p.m. for 60 s) were spin-coated on a Si handle wafer (test grade, 4science). After curing the PMMA and PI at 200 °C for 2 h, Al, which serves as the bottom electrode (350 nm thick), was deposited via thermal evaporation and patterned by photolithography and wet etching. A TiO_2 NM (66 nm thick) was then RF magnetron sputtered (base pressure of 5×10^{-6} torr, room temperature, deposition pressure of 5 mtorr, 20 s.c.c.m., 150 W RF power). Au NPs were synthesized separately and assembled on the TiO_2 NM surface via the Langmuir–Blodgett assembly process (see Supplementary section 'Materials and Methods'). A second TiO_2 NM (66 nm thick) was then deposited on the Au NPs in the same way as the first TiO_2 NM. An Al top electrode layer was deposited by thermal evaporation. This layer was also photolithographically patterned, completing the formation of a serpentine resistive memory. The PI precursor was then spin-coated to place the active layer near the neutral mechanical plane, and the entire device structure defined by a reactive ion etching (RIE) process using O_2 and SF_6 plasma (O_2 flow rate of 100 s.c.c.m., chamber pressure of 100 mtorr, 150 W RF power for 5 min; 50 s.c.c.m. of SF_6 flow rate, 55 mtorr, 250 W RF power for 4 min 30 s). After memory fabrication, the whole device (on the Si wafer) was dipped in boiling acetone to remove the sacrificial PMMA layer and release the PI-encapsulated device from the Si handle wafer. The memory was picked up with water-soluble tape (3M), and the device on the tape transfer-printed onto PDMS. Deionized water was used to dissolve the water-soluble tape to release the memory device, which was then transferred to the skin patch (Derma-Touch, Kwang Dong Pharmaceutical). Electrical measurements were carried out with a parameter analyser (B1500A, Agilent).

Fabrication of single-crystal Si NM strain sensor on the skin patch. Fabrication began by spin-coating PMMA and PI films onto a Si wafer. Photolithography and RIE (SF_6 plasma, 50 s.c.c.m., chamber pressure of 50 mtorr, 100 W RF power for 20 s) of a B-doped (doping concentration of $\sim 9.7 \times 10^{18}$ cm^{-3}) silicon-on-insulator (SOI) wafer formed 80-nm-thick Si NMs, which were transfer-printed onto the PI film. (Microscope images are shown in Supplementary Fig. 6.) Thermal evaporation was used for subsequent metallization (Cr/Au; 7 nm/70 nm thick), and the metal film then defined into specific patterns by photolithography and wet chemical etching. The top PI layer was then covered and the entire trilayer (PI/device/PI) patterned and etched by O_2 and SF_6 RIE. The entire device was released from the Si wafer by removing the PMMA sacrificial layer with acetone. Transfer printing of the released device to the skin patch completed the fabrication process.

© 2014 Macmillan Publishers Limited. All rights reserved.

Custom-made data processing and storage system. The sensing and data storage process begins by capturing physiological strain signals using onboard sensors, which can be stored locally in cells of non-volatile memory (Supplementary Fig. 7). A custom-made program written by Labview software (National Instruments) was used to process and store the recorded data. For example, in the case of strain sensing for the tremor model in motion-related neurological disorders (Fig. 5d), the frequencies of tremor, recorded by the onboard strain gauge, were analysed and classified into four different bands (0–0.5, 0.5–0.7, 0.7–0.9 and >0.9 Hz) by the program, which determined the appropriate compliance current and biasing voltage to write a specific two-digit code ([00], [01], [10] and [11], pre-assigned to each band) to the onboard wearable memory cells under multilevel-cell operation through the probe station.

Fabrication of electroresistive heater/temperature sensor on a skin patch. The skin-mountable heater was prepared by thermal evaporation of Cr/Au (10 nm/190 nm thick) through serpentine metal masks to define the serpentine shape on the non-adhesive side of the skin patch (opposite side to the hydrocolloid). After wiring, the heater was encapsulated in PDMS film. The same design and fabrication methods can be used for temperature sensors.

Other materials and methods. More detailed information about other materials and methods is provided in the Supplementary Information.

Received 9 October 2013; accepted 6 February 2014; published online 30 March 2014

References

1. Lobodzinski, S. S. & Laks, M. M. New devices for very long-term ECG monitoring. *Cardiol. J.* **19,** 210–214 (2012).
2. Stacey, W. C. & Litt, B. Technology insight: neuroengineering and epilepsy-designing devices for seizure control. *Nature Clin. Pract. Neurol.* **4,** 190–201 (2008).
3. Lotharius, J. & Brundin, P. Pathogenesis of Parkinson's disease: dopamine, vesicles and α-synuclein. *Nature Rev. Neurosci.* **3,** 932–942 (2002).
4. Kringelbach, M. L., Jenkinson, N., Owen, S. L. F. & Aziz, T. Z. Translational principles of deep brain stimulation. *Nature Rev. Neurosci.* **8,** 623–635 (2007).
5. Sekitani, T., Zschieschang, U., Klauk, H. & Someya, T. Flexible organic transistors and circuits with extreme bending stability. *Nature Mater.* **9,** 1015–1022 (2010).
6. Kim, D-H. *et al.* Stretchable and foldable silicon integrated circuits. *Science* **320,** 507–511 (2008).
7. Sekitani, T. *et al.* A rubberlike stretchable active matrix using elastic conductors. *Science* **321,** 1468–1472 (2008).
8. Kaltenbrunner, M. *et al.* An ultra-lightweight design for imperceptible plastic electronics. *Nature* **499,** 458–463 (2013).
9. Kim, D. K. *et al.* Flexible and low-voltage integrated circuits constructed from high-performance nanocrystal transistors. *Nature Commun.* **3,** 1216 (2012).
10. Viventi, J. *et al.* A conformal, bio-interfaced class of silicon electronics for mapping cardiac electrophysiology. *Sci. Transl. Med.* **2,** 24ra22 (2010).
11. Kim, D-H. *et al.* Materials for multifunctional balloon catheters with capabilities in cardiac electrophysiological mapping and ablation therapy. *Nature Mater.* **10,** 316–323 (2011).
12. Viventi, J. *et al.* Flexible, foldable, actively multiplexed, high-density electrode array for mapping brain activity *in vivo*. *Nature Neurosci.* **14,** 1599–1605 (2011).
13. Khodagholy, D. *et al. In vivo* recordings of brain activity using organic transistors. *Nature Commun.* **4,** 1575 (2013).
14. Kim, D-H. *et al.* Epidermal electronics. *Science* **333,** 838–843 (2011).
15. Takei, K. *et al.* Nanowire active-matrix circuitry for low-voltage macroscale artificial skin. *Nature Mater.* **9,** 821–826 (2010).
16. Chuan, W. *et al.* User-interactive electronic skin for instantaneous pressure visualization. *Nature Mater.* **12,** 899–904 (2013).
17. Lipomi, D. J. *et al.* Skin-like pressure and strain sensors based on transparent elastic films of carbon nanotubes. *Nature Nanotech.* **6,** 788–792 (2011).
18. Farra, R. *et al.* First-in-human testing of a wirelessly controlled drug delivery microchip. *Sci. Transl. Med* **4,** 122ra121 (2012).
19. Waser, R. & Aono, M. Nanoionics-based resistive switching memories. *Nature Mater.* **6,** 833–840 (2007).
20. Kwon, D-H. *et al.* Atomic structure of conducting nanofilaments in TiO_2 resistive switching memory. *Nature Nanotech.* **5,** 148–153 (2010).
21. Borghetti, J. *et al.* 'Memristive' switches enable 'stateful' logic operations via material implication. *Nature* **464,** 873–876 (2010).
22. Sekitani, T. *et al.* Organic nonvolatile memory transistors for flexible sensor arrays. *Science* **326,** 1516–1519 (2009).
23. Kang, N-G. *et al.* Structural and electrical characterization of a block copolymer-based unipolar nonvolatile memory device. *Adv. Mater.* **24,** 385–390 (2012).
24. Rogers, J. A., Lagally, M. G. & Nuzzo, R. G. Synthesis, assembly and applications of semiconductor nanomembranes. *Nature* **477,** 45–53 (2011).
25. Prausnitz, M. R. & Langer, R. Transdermal drug delivery. *Nature Biotechnol.* **26,** 1261–1268 (2008).
26. Sungho, K. & Choi, Y-K. A comprehensive study of the resistive switching mechanism in Al/TiO_x/TiO_2/Al-structured RRAM. *IEEE Trans. Electron. Dev.* **56,** 3049–3054 (2009).
27. Tao, A. R., Huang, J. & Yang, P. Langmuir–Blodgettry of nanocrystals and nanowires. *Acc. Chem. Res.* **41,** 1662–1673 (2008).
28. Talapin, D. V., Lee, J-S., Kovalenko, M. V. & Shevchenko, E. V. Prospects of colloidal nanocrystals for electronic and optoelectronic applications. *Chem. Rev.* **110,** 389–458 (2009).
29. Lu, X., Tuan, H-Y., Korgel, B. A. & Xia, Y. Facile synthesis of gold nanoparticles with narrow size distribution by using AuCl or AuBr as the precursor. *Chem. Eur. J.* **14,** 1584–1591 (2008).
30. Yamada, Y. *et al.* Nanocrystal bilayer for tandem catalysis. *Nature Chem.* **3,** 372–376 (2011).
31. Shang, D. S. *et al.* Effect of carrier trapping on the hysteretic current–voltage characteristics in $AgLa_{0.7}Ca_{0.3}MnO_3Pt$ heterostructures. *Phys. Rev. B* **73,** 245427 (2006).
32. Kim, K. M. *et al.* A detailed understanding of the electronic bipolar resistance switching behavior in Pt/TiO_2/Pt structure. *Nanotechnology* **22,** 254010 (2011).
33. Jeong, H. Y. *et al.* Interface-engineered amorphous TiO_2-based resistive memory devices. *Adv. Funct. Mater.* **20,** 3912–3917 (2010).
34. Lee, J. E. *et al.* Multifunctional mesoporous silica nanocomposite nanoparticles for theranostic applications. *Acc. Chem. Res.* **44,** 893–902 (2011).
35. Peer, D. *et al.* Nanocarriers as an emerging platform for cancer therapy. *Nature Nanotech.* **2,** 751–760 (2007).
36. Kim, T.-i. *et al.* Injectable, cellular-scale optoelectronics with applications for wireless optogenetics. *Science* **340,** 211–216 (2013).
37. Sekitani, T. *et al.* A large-area wireless power-transmission sheet using printed organic transistors and plastic MEMS switches. *Nature Mater.* **6,** 413–417 (2007).

Acknowledgements

This work was supported by the Institute for Basic Science. This work was also supported by a grant (2013M3A6A5073180) from the Center for Advanced Soft Electronics under the Global Frontier Research Program of the Ministry of Science, ICT and Future Planning, Korea, and by a grant from the Basic Science Research Program of the National Research Foundation of Korea (NRF), funded by the Ministry of Science, ICT and Future Planning (2012R1A1A1004925). N.L. acknowledges startup funding from the Cockrell School of Engineering of the University of Texas at Austin. C.S.H. acknowledges support from the Global Research Laboratory Program (2012040157) through the NRF.

Author contributions

D.S., J.L. and D-H.K. designed the experiments. D.S., J.L., S.Q., R.G., J.K., S.J.K., S.Y., C.S., J.E.L., D.J.L., S.W.J., M.P., J.S., K.D., M.L., K.K., C.S.H., N.L., T.H. and D-H.K. performed experiments and analysis. D.S., J.L., S.Q., J.L., R.G., J.K., C.S.H., N.L., T.H. and D-H.K. wrote the paper.

Additional information

Supplementary information is available in the online version of the paper. Reprints and permissions information is available online at www.nature.com/reprints. Correspondence and requests for materials should be addressed to D.H.K.

Competing financial interests

The authors declare no competing financial interests.

© 2014 Macmillan Publishers Limited. All rights reserved.

nature nanotechnology

SUPPLEMENTARY INFORMATION

DOI: 10.1038/NNANO.2014.38

Multifunctional wearable devices for diagnosis and therapy of movement disorders

Donghee Son[1,2⊥], Jongha Lee[1,2⊥], Shutao Qiao[3], Roozbeh Ghaffari[4], Jaemin Kim[1,2], Ji Eun Lee[1,2], Changyeong Song[1,2], Seok Joo Kim[1,2], Dong Jun Lee[1,2], Samuel Woojoo Jun[1,2], Shixuan Yang[3], Minjoon Park[1,2], Jiho Shin[1,2], Kyungsik Do[1,2], Mincheol Lee[1,2], Kwanghun Kang[1,2], Cheol Seong Hwang[5], Nanshu Lu[3], Taeghwan Hyeon[1,2], Dae-Hyeong Kim[1,2]*

[⊥]*D. Son and J. Lee contributed equally.*

*To whom correspondence should be addressed. *E-mail: dkim98@snu.ac.kr*

© 2014 Macmillan Publishers Limited. All rights reserved.

1. Supplementary Text

1.1. Detailed switching mechanism of the wearable memory.

The bipolar switching characteristics in I-V curves of RRAM can be attributed to the accumulation and depletion of oxygen. This accumulation and depletion depend on the bias polarity near the interface between top Al electrode and TiO_2 switching layer, where the oxygen-deficient TiO_x layer is formed (Supplementary Fig. S10, top). The interface between the bottom Al electrode and TiO_2 switching layer remains intact due to the presence of more stable AlO_x layer (Supplementary Fig. S10, bottom). Many RRAM devices are activated by the electroforming process, which makes conduction paths between cathode and anode. However, the initial set voltage of TiO_2-based memories is similar with following set voltages, and therefore, there is no need of the electroforming process. Additionally, Au NPs in TiO_2/Au NPs/TiO_2 structure produces charge trap sites[1], by which the low current level in MINIM can be explained. However, Au NPs are surrounded by alkyl chains (oleylamine ligands) and these ligands may also generate the charge trap sites. To clarify this ligand effect on the formation of charge trap sites, SAM (stearic acid, which is similar to oleylamine ligands) is used to functionalise TiO_2 NM surface (MISIM structure, Supplementary Fig. S3). However, MISIM structure did not show the decrease of switching current (Fig. 3a). Consequently, the ligand effect is negligible for the generation of charge trap sites. On the contrary, the increase of the number of Au NPs layers in the MINIM structure from one layer to three layers decreases the switching current further (Fig. 3a). As a result, the number of layers of Au NPs is important for controlling the operation current, while the ligands have minimal influences.

1.2. Reliability tests (endurance, retention) of the wearable memory

The endurance operation is conducted by consecutive DC voltage sweeping from -4 V to 3 V. Each of high-resistance state (HRS) and low-resistance state (LRS) currents measured at the read voltage of -0.5 V shows stable operation (Fig. 3e, S3). In retention measurements, the individual resistance states are programmed by DC voltage bias. The high-resistance state (HRS) and low-resistance state (LRS) states are well sustained at read voltage of -0.5 V.

1.3. Cumulative probability plots of high-resistance state (HRS) and low-resistance state (LRS) in MIM and MINIM

Cumulative probability is a critical parameter in verifying the uniformity of resistive switching operation. Cumulative probabilities of high-resistance state (HRS) and low-resistance state (LRS) resistances are measured under compliance currents of 1 mA and 50 μA in 50 cells of the array,

© 2014 Macmillan Publishers Limited. All rights reserved.

respectively. The on/off ratio between high-resistance state (HRS) and low-resistance state (LRS) in MIM and MINIM is approximately 10. Both MIM and MINIM show a good uniformity within the array.

1.4. Finite element modelling (FEM) of the strain distribution of stretchable memory

Multilayer stretchable memories are modelled as shell elements of multiple integration points in commercial finite element software ABAQUS. The elastomer substrate is modelled using 3D elements which bonds to only the intersections of the serpentine network. Strain distribution after 25% horizontally applied strain is shown in Fig. 4i and Supplementary Fig. S5. The maximum strain stayed below 0.008% in the intersection (switching layer, TiO_2 NM) and below 0.04% in the serpentine interconnects, which are both far below the failure strain of inorganic oxides (~1%).

1.5. Analytical modelling of the gauge factor of Si strain sensor.

The Si strain gauges are modelled as 2D plane strain problem. When the substrate is subjected to a uniform tensile strain ε_{app}, the normalised average strain in the Si NM is predicted to be

$$\frac{\varepsilon_{avg}}{\varepsilon_{app}} = \frac{\overline{E}_s H}{\overline{E}_{Si} h_{Si} + \overline{E}_{PI} h_{PI} + \overline{E}_s H} \quad \text{(S1)},$$

where $\overline{E}_s$, H, $\overline{E}_{Si}$, h_{Si} and $\overline{E}_{PI}$, h_{PI} are the plane strain modulus and thickness of the substrate, Si and polyimide respectively. The substrate is 40:1 PDMS (E_s = 48 kPa) with a thickness of H = 1.5 mm. The Si NM with a thickness h_{Si} = 80 nm is along the <110> direction with doping concentration (p-type) of 9.7×10^{18} /cm^3, hence E_{Si} = 168 GPa, GF_{Si} = 112. The Si NM is sandwiched between two identical polyimide (E_{PI} = 2.5 GPa) layers of total thickness h_{PI} = 2.4 mm. With above parameters, $\varepsilon_{avg} / \varepsilon_{app}$ is calculated to be 0.0045. Hence the effective gauge factor of the stretchable strain gauge is given by

$$\mathrm{GF} = \mathrm{GF}_{Si} \frac{\varepsilon_{avg}}{\varepsilon_{app}} = 112 \times 0.0045 = 0.5 \quad \text{(S2)},$$

which is in good match with the experimental measurement (Fig. 5b).

© 2014 Macmillan Publishers Limited. All rights reserved.

1.6. FEM of 3D thermal profile of the resistive heater.

Finite element simulations have been performed via COMSOL 4.2 to determine the temperature distribution when the wearable heater is turned on to accelerate the transdermal drug delivery. The skin is modelled as a multilayer substrate with different thermal properties in each layer as illustrated in Supplementary Fig. S9a[2]. Thickness (h), heat capacity (C), heat conductivity (k), density (ρ), blood perfusion rate (ω_b) and metabolic heat generation (Q) of each skin layer used in our model are given in Supplementary Table S1.

	H (mm)	C (J kg^{-1} K^{-1})	K (W m^{-1} K^{-1})	ρ (kg m^{-3})	ω_b (s^{-1})	Q (W m^{-3})
Epidermis	0.1	3589	0.235	1200	0	0
Papillary dermis	0.7	3300	0.445	1200	0.0002	368.1
Reticular dermis	0.8	3300	0.445	1200	0.0013	368.1
Fat	2	2674	0.185	1000	0.0001	368.3
Muscle	8	3800	0.51	1085	0.0027	684.2

Table S1. Normal themophysical property values and layer thicknesses of the skin.

The governing equation of the heat transfer in each skin layer is:

$$\rho C \frac{\partial T}{\partial t} = k\nabla^2 T + \rho_b C_b \omega_b (T_b - T) + Q \quad \text{(S3)},$$

where $\rho_b = 1060\ kg/m^3$ and $C_b = 3770\ \mathrm{J/kg}\,m^3$ represent the mass density and the heat capacity of blood, respectively. As for the skin patch and the PDMS encapsulation, there is no blood perfusion or heat source. Therefore, equation (S3) decays to the basic heat transfer model in solids:

$$\rho C \frac{\partial T}{\partial t} = k\nabla^2 T \quad \text{(S4)},$$

with material properties listed in Supplementary Table S2. The Joule heating model for the heater is given by

$$\rho C \frac{\partial T}{\partial t} = k\nabla^2 T + \sigma(\nabla V)^2 \quad \text{(S5a)},$$

and

$$\varepsilon_0 \varepsilon_r \frac{\partial}{\partial t}(\nabla^2 V) = -\sigma \nabla^2 V \quad \text{(S5b)},$$

where V is the electrical potential, σ and ε_r denote the electrical conductivity and the relative

© 2014 Macmillan Publishers Limited. All rights reserved.

permittivity of the heater material, respectively. The heater properties listed in Supplementary Table S2 are calibrated using the experimental results given in Fig. 6b, which shows the surface temperature distribution of the heater fabricated on a glass slide obtained from an infrascope. If DC power is supplied, $\partial V / \partial t = 0$.

	h (mm)	C (J kg^{-1} K^{-1})	K (W m^{-1} K^{-1})	ρ (kg m^{-3})	σ (S m^{-1})	ε_r
PDMS encap.	0.1	1200	0.17	965	-	-
Heater	0.05	129	317	19.3×10^{3}	1.395×10^{7}	1
Skin patch (PU)	0.4	3100	0.2	1100	-	-

Table S2. Thermo-physical property values of PDMS capsulation, heater and skin patch.

Skin is considered infinitely large such that open boundary conditions are applied to lateral surfaces. Temperature at the bottom surface of muscle layer is set to equal the core temperature of T_b = 37 °C. Convective cooling between the surface of the PDMS encapsulation layer and the environment is taken into consideration as well as the effect of the surface-to-ambient radiation. The environmental temperature is measured to be 15 °C. By applying the Joule heating model, equation (S5), in the heater and the heat transfer model, equations (S3) and (S4), in other parts, we can simulate the heat generated in the heater due to Joule effect being transferred through the skin patch to the skin in both transient and stationary states. The stationary state can be simply degenerated from equation (S3) by setting $\partial T / \partial t = 0$. Supplementary Fig. S9b displays the 3D temperature distribution of the skin in stationary state. The maximum temperature at the patch-skin interface is 49.2 °C in the stationary state when the heater is supplied with a power of 0.23 W. Figure 6c displays the 3D temperature distribution after 20 minutes heating using the transient model and Fig. 6g plots the temperature profile as a function of time. The red curve shows the maximum temperature in the heater which is located at the top surface of the patch, while the orange curve represents the maximum temperature at the patch-skin interface. As we can see from the plot, after the skin patch being heated for 10 minutes, the temperature in the patch/skin interface reaches a plateau and then increases slowly as heating time increases (less than 0.5 °C/min). If we set the safe temperature of the human skin (the temperature at the bottom of epidermis layer) to be 45 °C, we can keep supplying power to the heater for 20 minutes without burning the skin. The blue curve also shows the diffusivity of the drug for the transdermal drug delivery, which increases exponentially as the temperature increases.

© 2014 **Macmillan Publishers Limited. All rights reserved.**

1.7. Diffusion of Rhodamine B dyes into the pig skin as a simulated transdermal drug delivery.

Rhodamine B dyes (≥95%, Sigma Aldrich, USA) are loaded on m-silica NPs, which are transfer-printed to the hydrocolloid side of the skin patch. The skin patch is applied to the prepared pig skin (size of 1.5 cm × 1.5 cm). Two groups of samples are prepared. One group is placed under the room temperature (25 °C) while the other group is continuously heated at 40 °C up to 60 minutes. Then, pig skins of each group are put into the freezer (-80 °C) for 20 minutes to terminate the diffusion of Rhodamine B dyes. The specimens are frozen in optimal cutting temperature (OCT) compound (Leica, 3801480, Nussloch, Germany) at -80 °C. Then the frozen samples are sectioned into 15 μm-thick slices by using a Cryostat Cryocut Microtome (Leica, CM1510S, Nussloch, Germany). The diffusion depth of dyes into the pig skin samples are measured with a fluorescence microscope (Nikon, Eclipse Ti, Tokyo, Japan).

1.8. Flexible wiring that connects devices to external equipment.

For the operation of the power supply and the control of the multifunctional wearable system, the external equipment is connected through flexible cables (anisotropic conductive films, ACFs). Several previous reports[3,4] have shown the ACF connection is robust and reliable even under severe mechanical deformations. ACF cables connect the proposed system to external equipment (data acquisition system and parameter analyser) through the custom made PCB board. A custom-made Labview-based software controls the data acquisition system and the general purpose interface bus (GPIB) with the parameter analyser.

© 2014 Macmillan Publishers Limited. All rights reserved.

2. Materials and Methods

2.1. Synthesis of Au NPs.

Au NPs are prepared via modification of previously reported procedures[5]. In the typical synthesis, 0.4 g of $HAuCl_4 \cdot 3H_2O$ (99.9%, Strem, USA), 10 mL of oleylamine (Acros, 90%, USA), and 30 mL of 1-octadecene (90%, Sigma Aldrich, USA) are mixed in a 50 mL glass vial at the room temperature. The vial is placed on an oil bath and heated up to 90 °C. The solution is heated for 2 hours, and then the NPs are precipitated and washed with ethanol twice, followed by centrifugation. The precipitated NPs are redispersed with 5 mL of chloroform.

2.2. Characterisation of Au NPs.

The samples for the TEM analysis are prepared by dropping a solution containing Au NPs on the surface of a copper grid coated with amorphous carbon film. The TEM images are collected on a JEM-2010 (JEOL, Japan) electron microscope operated at an accelerating voltage of 200 kV. The UV-Vis absorption spectra are taken with a Cary V-550 UV-VIS-NIR (Agilent, USA) spectrophotometer.

2.3. Langmuir-Blodgett assembly of Au NPs.

Oleylamine-capped Au NPs are dispersed in chloroform (50 mg/mL). This solution is dropped onto the water sub-phase of a Langmuir-Blodgett trough (IUD 1000, KSV instrument, Finland). After the evaporation of the solvent, the surface layer becomes compressed by the mobile barriers (5 mm/min). After a surface pressure of 30 mN/m is achieved, the Au NPs are deposited onto the substrate by lifting it up and dipping down at 1 mm/min.

2.4. Measurement of I-V curves during mechanical stretching experiments.

Stretching experiments are performed with an automatic stretching stage, which can apply tensile or compressive strains in the *x* and *y* directions. With the edges of the electronic patch clamped to the stage, the electrical measurements are performed with the probe station and parameter analyser (B1500A, Agilent, USA), while generating tensile/compressive deformations.

2.5. Synthesis of mesoporous silica (m-silica) NPs.

Functional molecules, i.e. drugs, can be loaded into the m-silica NPs for therapeutic applications. Monodisperse m-silica NPs are synthesised using the previously reported method[6]. NaOH (0.35 mL, 2 M, 98%, Sigma Aldrich, USA) is added to 50 mL of cetyltrimethylammonium

© 2014 Macmillan Publishers Limited. All rights reserved.

bromide (CTAB, > 99%, Acros, USA) solution (100 mg in 50 mL of water). The mixture is heated to 70 °C, and then 0.5 mL tetraethylorthosilicate (TEOS, 98%, Acros, USA) is added. After 1 minute, 0.5 mL of ethyl acetate (99.5%, Samchun, Korea) is added, and the resulting mixture is stirred at 70 °C for 30 s and then aged for 2 h. The resulting precipitate is collected by centrifugation and washed with copious water and ethanol. Finally, the pore-generating template, CTAB, is removed by refluxing in acidic ethanol solution.

2.6. Characterisation of m-silica NPs.

A JEM-2010 transmission electron microscope (JEOL, Japan) is used for transmission electron microscopy (TEM) analysis. N_2 adsorption and desorption isotherms are measured at 77 K using a Micromeritics ASAP 2000 gas adsorption analyser. The surface area and the total pore volume are determined using the Brunauer–Emmett–Teller equation and the Barrett-Joyner-Halenda method, respectively.

2.7. Loading of Rhodamine B onto m-silica NPs.

As a drug diffusion model, Rhodamine B (≥95%, Sigma Aldrich, USA) is loaded on m-silica NPs. Rhodamine B solution (0.2 mL, 20 mg/mL in methanol) is adsorbed on the surface of m-silica NPs (0.15 g). Rhodamine B loaded in m-silica NPs are dried at room temperature.

2.8. Fabrication of structured PDMS stamp for transfer printing drug-loaded m-silica NPs.

Negative photoresist (SU8-25, Microchem, USA) is spin-coated on the pre-cleaned and O_2 plasma-treated Si wafer. Photolithography is conducted on spin-coated SU8 to pattern holes that are 40 μm deep, 600 μm wide, and 1.46 mm spaced. Next, the SU8 mould is placed in a dish, which is heated on a 150 °C hot plate to promote the adhesion between the mould and the Si wafer. 10:1 PDMS (Sylgard 184A:Sylgard 184B, Dow Corning, USA) is then poured into the dish. After 24 h, the cured structured PDMS stamp with the micro-dot array is slowly detached from the SU8 mould (Supplementary Fig. S8b).

2.9. Transfer printing drug-loaded m-silica NPs onto skin patch.

The drug-loaded (or dye-loaded) m-silica NPs solution is dropped on the surface of the structured PDMS stamp. The stamp is dried for ~20 minutes. The dried dye-loaded m-silica NPs are transfer printed as a microdot array to the hydrocolloid side of the skin patch (Supplementary Fig. S8a).

© 2014 Macmillan Publishers Limited. All rights reserved.

2.10. Temperature distribution measurement of the heater by using an infrared camera.

The wavy-patterned Cr/Au-based heater (10 nm/190 nm, line width of 300 μm, 95.9 Ω) on a 1 mm-thick slide glass is connected to the power source (12 V, 1.5 W) under 15 °C surrounding temperature. The time-dependent thermo-grams are captured by the thermographic camera (320×240 pixels, IRE Korea, Korea), and the maximum temperature of the heater is plotted.

3. References

1. Han, S., *et al.* Microcontact printing of ultrahigh density gold nanoparticle monolayer for flexible flash memories. *Adv. Mater.* **24**, 3356-3561 (2012).
2. Çetingül, M. P. & Herman. C. A heat transfer model of skin tissue for the detection of lesions: sensitivity analysis. *Phys. Med. Biol.* **55**, 5933-5951 (2010).
3. Kim, D.-H., *et al.* Materials for multifunctional balloon catheters with capabilities in cardiac electrophysiological mapping and ablation therapy. *Nature Mater.* **10,** 316-323 (2011).
4. Kim, D.-H., *et al*. Epidermal electronics. *Science* **333**, 838-843 (2011).
5. Lu, X., Tuan, H.-Y., Korgel, B. A. & Xia, Y. Facile synthesis of gold nanoparticles with narrow size distribution by using AuCl or AuBr as the precursor. *Chem. Eur. J.* **14**, 1584-1591 (2008).
6. Lee, J. E. *et al*. Uniform mesoporous dye-doped silica nanoparticles decorated with multiple magnetite nanocrystals for simultaneous enhanced magnetic resonance imaging, fluorescence imaging, and drug delivery. *J. Am. Chem. Soc.* **132**, 552-557 (2009).

© 2014 **Macmillan Publishers Limited. All rights reserved.**

Supplementary Figure Legends

Figure S1. Schematic illustration of the operation process of the wearable bio-integrated system: wearable strain sensor detects movement disorders, the recorded data are stored in onboard memory modules, diagnostic patterns are analyzed on the basis of the stored data stream, thermal actuators apply heat to drug-loaded m-silica NPs, drugs are diffused transdermally, and movement disorders can be treated.

Figure S2. Schematic overview of the fabrication process of the wearable memory array.

Figure S3. Contact angles of the native TiO_2 surface (left) and SAM-modified TiO_2 surface (right).

Figure S4. I-V characteristics and reliability data of the wearable memory. **a,** I-V characteristics of the MISIM structure with the compliance current < 100 atte**b,** Reliability (endurance and retention) measurement of MIM and **c,** MISIM structure. **d,** Multi-level cell (MLC) operation of the MISIM structure.

Figure S5. Finite element modelling (FEM) analysis of the strain distribution in active layer (TiO_2 NM) under ~25% external strain.

Figure S6. Microscope images of fabrication steps of the stretchable Si strain sensor.

Figure S7. Overview of the custom-made data processing and storage system.

Figure S8. a, Schematic overview of transfer printing process of drug-loaded m-silica NPs, sensors and memory devices. **b,** Image of the structured PDMS stamp used in the transfer printing process.

Figure S9. a, Schematic sectional view of the electronic patch mounted on the skin. **b,** FEM analysis of the temperature distribution at the skin/patch interface (on the skin).

Figure S10. TEM images of switching layers: TiO_x between the top Al electrode and TiO_2 NM switching layer (top) and AlO_x between the bottom Al electrode and TiO_2 NM switching layer (bottom).

© 2014 **Macmillan Publishers Limited. All rights reserved.**

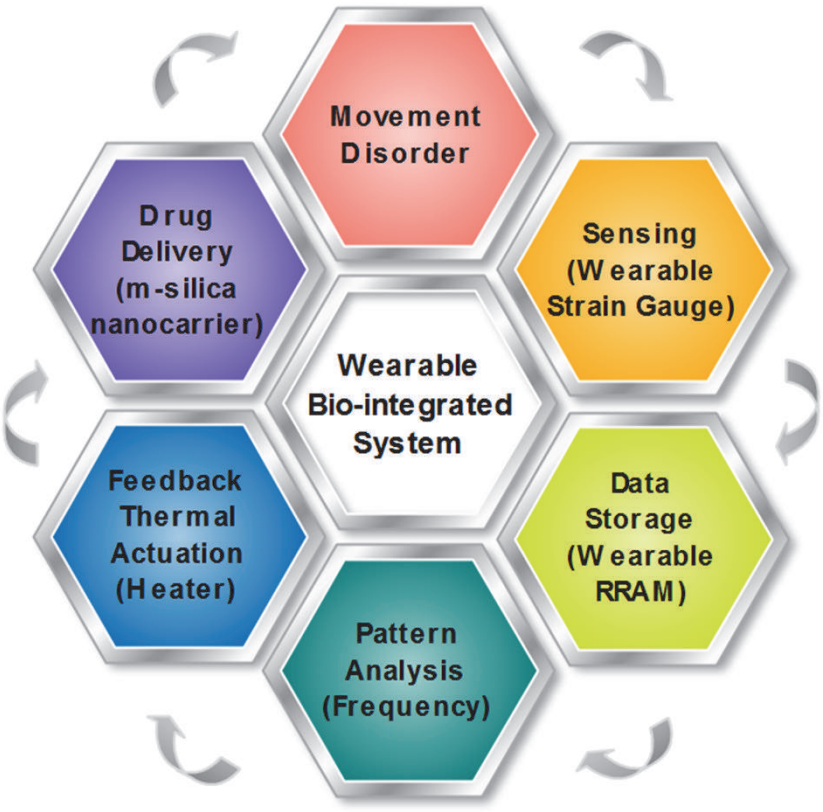

Supplementary Fig. S1

© 2014 Macmillan Publishers Limited. All rights reserved.

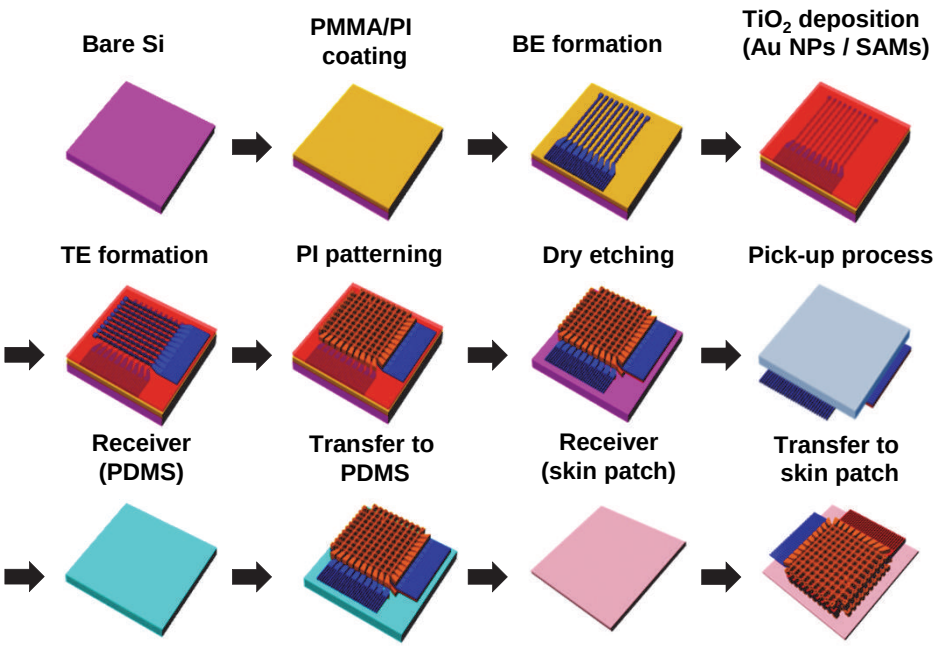

Supplementary Fig. S2

© 2014 Macmillan Publishers Limited. All rights reserved.

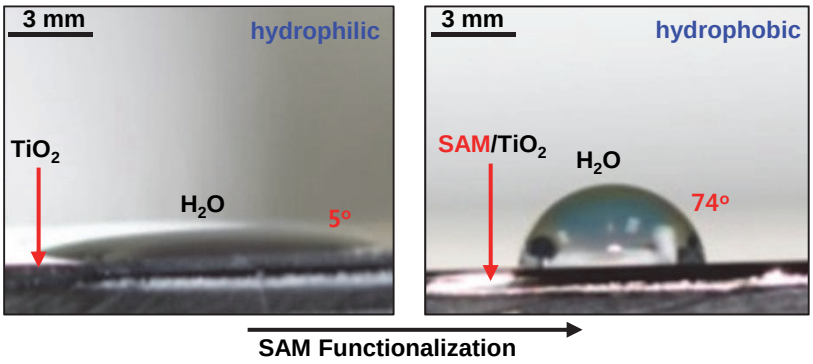

Supplementary Fig. S3

© 2014 Macmillan Publishers Limited. All rights reserved.

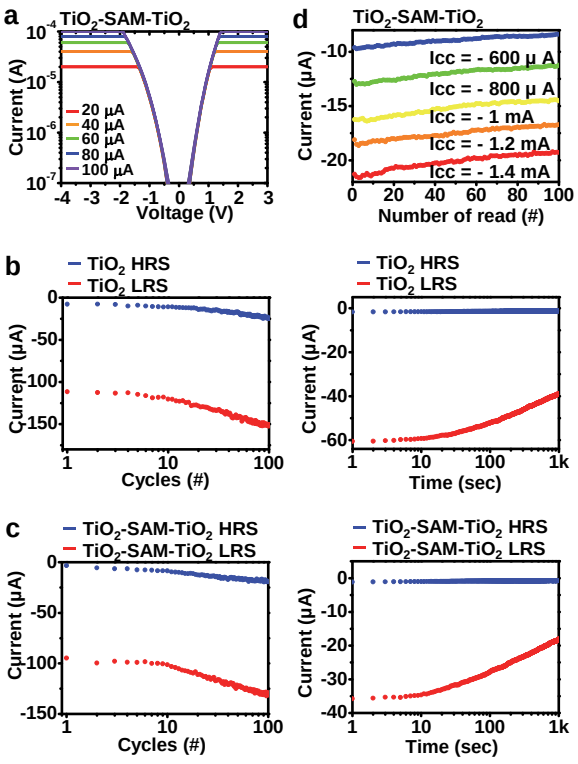

Supplementary Fig. S4

© 2014 Macmillan Publishers Limited. All rights reserved.

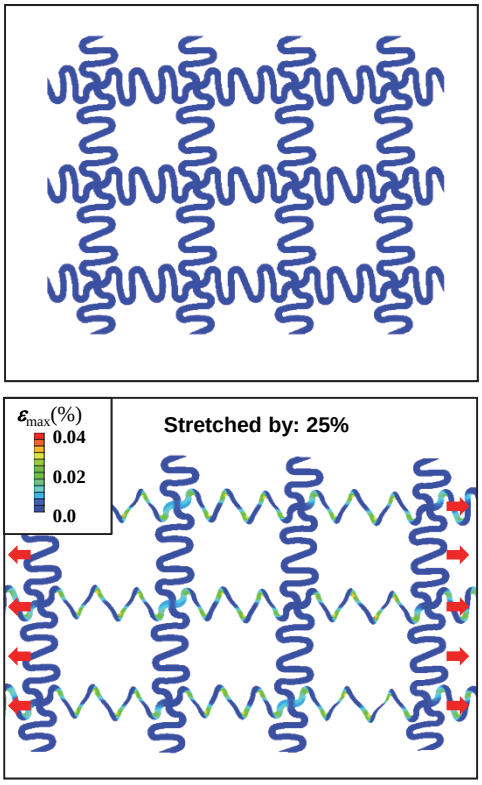

Supplementary Fig. S5

© 2014 Macmillan Publishers Limited. All rights reserved.

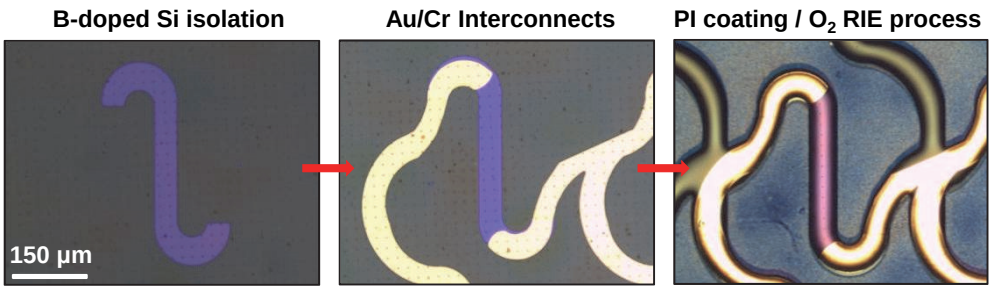

Supplementary Fig. S6

© 2014 Macmillan Publishers Limited. All rights reserved.

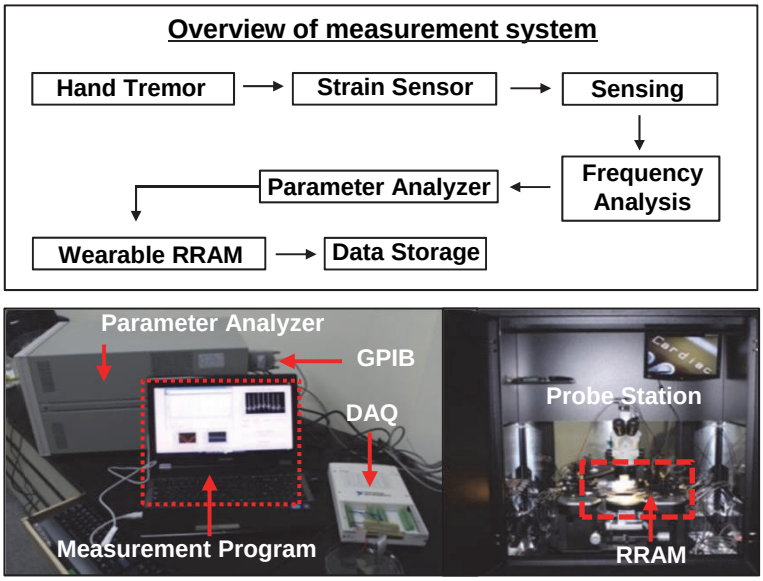

Supplementary Fig. S7

© 2014 Macmillan Publishers Limited. All rights reserved.

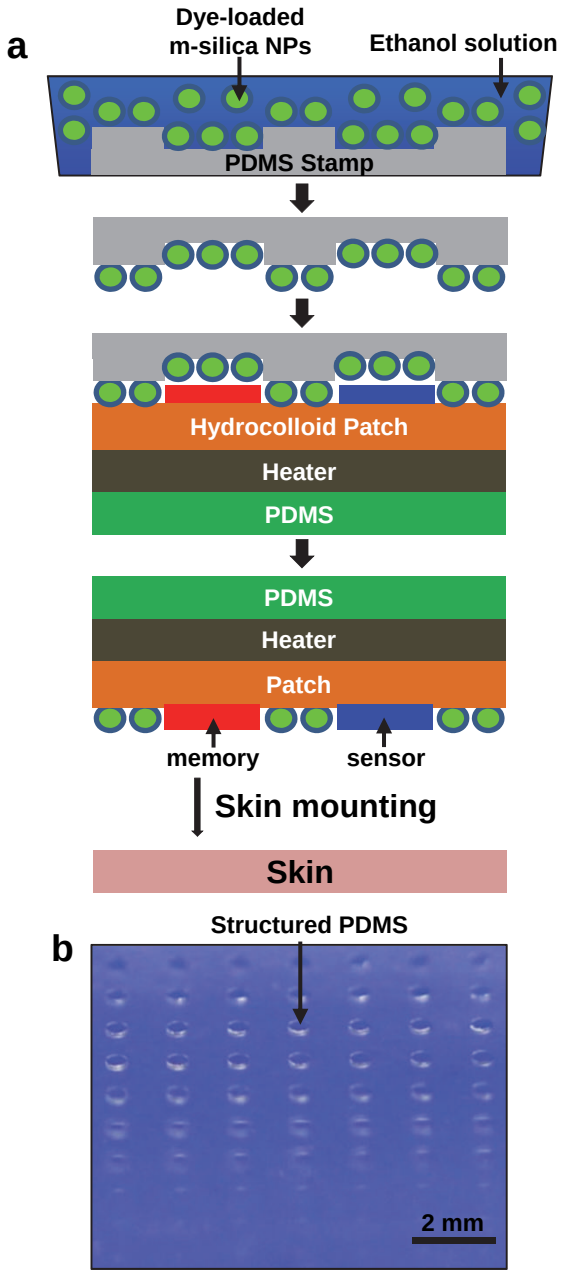

Supplementary Fig. S8

© 2014 Macmillan Publishers Limited. All rights reserved.

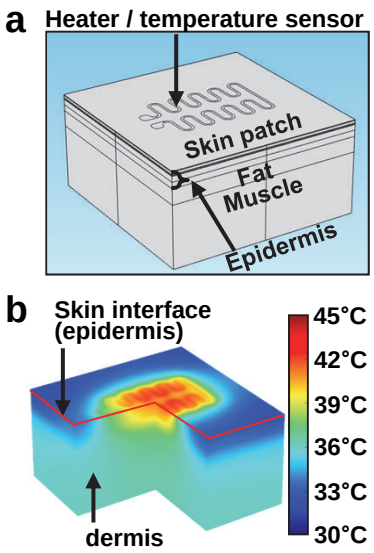

Supplementary Fig. S9

© 2014 Macmillan Publishers Limited. All rights reserved.

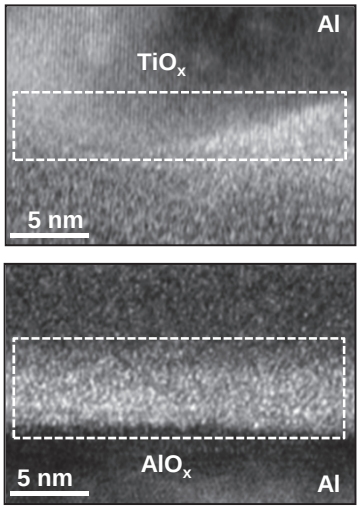

Supplementary Fig. S10

© 2014 **Macmillan Publishers Limited. All rights reserved.**